Bioactive Materials 25 (2023) 580–593

Contents lists available at ScienceDirect

Bioactive Materials

journal homepage: www.keaipublishing.com/en/journals/bioactive-materials

Activation of pyroptosis by specific organelle-targeting photodynamic therapy to amplify immunogenic cell death for anti-tumor immunotherapy

Shuang Zeng [a,1], Chen Chen [b,1], Liuwei Zhang [a], Xiaosheng Liu [a], Ming Qian [a], Hongyan Cui [a], Jingyun Wang [a,*], Qixian Chen [a,**], Xiaojun Peng [b]

[a] School of Bioengineering, Dalian University of Technology, 2 Linggong Road, Hi-tech Zone, Dalian, 116024, China
[b] State Key Laboratory of Fine Chemicals, Dalian University of Technology, 2 Linggong Road, Hi-tech Zone, Dalian, 116024, China

ARTICLE INFO

Keywords:
Pyroptosis
Tumor
Photodynamic therapy
Immunogenic cell death
Subcellular targeting

ABSTRACT

Pyroptosis, a unique lytic programmed cell death, inspired tempting implications as potent anti-tumor strategy in pertinent to its potentials in stimulating anti-tumor immunity for eradication of primary tumors and metastasis. Nonetheless, rare therapeutics have been reported to successfully stimulate pyroptosis. In view of the intimate participation of reactive oxygen species (ROS) in stimulating pyroptosis, we attempted to devise a spectrum of well-defined subcellular organelle (including mitochondria, lysosomes and endoplasmic reticulum)-targeting photosensitizers with the aim of precisely localizing ROS (produced from photosensitizers) at the subcellular compartments and explore their potentials in urging pyroptosis and immunogenic cell death (ICD). The subsequent investigations revealed varied degrees of pyroptosis upon photodynamic therapy (PDT) towards cancerous cells, as supported by not only observation of the distinctive morphological and mechanistic characteristics of pyroptosis, but for the first-time explicit validation from comprehensive RNA-Seq analysis. Furthermore, *in vivo* anti-tumor PDT could exert eradication of the primary tumors, more importantly suppressed the distant tumor and metastatic tumor growth through an abscopal effect, approving the acquirement of specific anti-tumor immunity as a consequence of pyroptosis. Hence, pyroptosis was concluded unprecedently by our proposed organelles-targeting PDT strategy and explicitly delineated with molecular insights into its occurrence and the consequent ICD.

1. Introduction

Cancer, owing to its inherent complication in pathophysiology and formidable malignancy in invading the neighboring tissues and extravasating for tumorigenesis at the distant sites, remains the clinical challenge and accounts for one of the most human mortalities [1,2]. In addition to the surgical interventions, chemotherapy prevails as the first-line clinical regime in suppressing cancer progression. Note that the pharmacological schemes of most intensively-used chemotherapeutics are intended for apoptosis, nonetheless, inherent or acquired multi-resistance of cancerous cells to apoptosis (particularly subjected to multiple circles of chemotherapy) underpins the failure of clinical chemotherapy [3–5]. Moreover, apoptosis is acknowledged to be non-immunogenic, and the ensuing apoptotic proceedings are stealthily confined in the cell interiors. Hence, to avert the intrinsic handicaps of apoptosis, it is rationale to contrive alternative cell death pathways rather than this silent apoptosis and inflame the immunological dormancy for pronounced immunogenic cell death (ICD) and activated anti-tumor immunities for complete eradication of cancerous cells.

Pyroptosis is a lytic programmed cell death, initially recognized as a mechanism of anti-microbial host defense and of outflux of immunostimulatory cytokines (*e.g.,* interleukin-1β and interleukin-18) [6,7]. Pyroptosis is schemed to exaggerate ICD by means of uncontrolled release of intracellular pro-inflammatory contents [*e.g.,* lactate dehydrogenase (LDH), inflammatory cytokines including interleukin-1β (IL-1β) and interleukin-18 (IL-18)] [8,9]. Hence, the pro-inflammatory programmed pyroptosis is presumed to not inflict apoptosis-associated drug-resistance, more importantly, which could also stimulate ICD and

Peer review under responsibility of KeAi Communications Co., Ltd.
* Corresponding author.
** Corresponding author.
E-mail addresses: wangjingyun67@dlut.edu.cn (J. Wang), qixian@dlut.edu.cn (Q. Chen).
[1] These authors contributed equally to this work and should be considered co-first authors.

https://doi.org/10.1016/j.bioactmat.2022.07.016
Received 10 March 2022; Received in revised form 5 July 2022; Accepted 13 July 2022
Available online 2 August 2022

facilitate the prime of immunity to the pyroptotic cells [10–14]. To date, pyroptosis is primarily observed in the promoted clearance of infection by viral, bacterial, fungal, and protozoan and barely reported from several chemotherapeutic drugs [15–17]. Exceptional high spatiotemporal concentrations of chemotherapeutic drugs in the cell interiors were reported to initiate pyroptosis, however, exceedingly high dosage of chemotherapeutic drugs could induce acute off-target toxicity. To circumvent this obstacle, we are encouraged to contrive a potent and spatiotemporal precision approach to activate pyroptosis and investigate its potentials in stimulating ICD and thereby eradication of intractable tumors.

Photodynamic therapy (PDT) has gained clinical appreciation in treatment of a number of intractable tumors due to its high spatiotemporal precision, minimal invasiveness and unlikely acquirement of PDT resistance [18–21]. In principle, PDT is achieved by excitation of photosensitizing chemicals (photosensitizers) in molecular oxygen-presenting atmosphere to stimulate photochemical reactions in production of detrimental reactive oxygen species (ROS), particularly singlet oxygen, with the intention of eliciting irreversibly cytocidal consequence [22–26]. Given that recent researches on molecular biology of pyroptosis disclosed the crucial participation of ROS in inflammasome activation (NLRP3) [27], for instance, Nakahira et al. and Shimada et al. reported oxidized mitochondrial DNA that is released from destructive mitochondria can directly bind to and activate the NLRP3 inflammasomes [28,29], and Zhou et al. suggested that Thioredoxin and Thioredoxin-interacting protein could respond the oxidative stress and commit binding to the NLRP3 inflammasomes [30]. To these respects, it is very intriguing to interrogate the possibilities of PDT in inducing pyroptosis. Moreover, in view of ROS produced by PDT susceptible to rapid elimination (ultrashort lifetime: 20–40 ns; effective coverage: 20 nm) [31–33], as well as the aforementioned pyroptotic signaling pathways starting from oxidization in specific subcellular organelles, we are motivated to elaborate an array of vital subcellular organelles (mitochondria, lysosomes, endoplasmic reticulum)-targeting photosensitizers, aiming to localize PDT for maximized activation of inflammasomes and the consequent pyroptosis.

In this article, we would like to report for the first time that PDT precisely aiming at specific subcellular organelles can lead to pyroptosis, and the ROS-mediated organelle damage promotes the activation of pyroptosis-specific caspases (caspase 1) and commitment of hydrolysis and liberation of pore-forming gasdermins (GSDMD-N) for the rupture of plasma membranes, which facilitates the release of intracellular contents (LDH et al.) and promotes abundant and large-scale ICD (Scheme 1). The molecular design of subcellular target photosensitizers referred to be **Mito-ZS**, **Lyso-ZS**, and **ER-ZS**, respectively (Fig. 1A), which was rooted from the same parental cyanine chromophore [34], followed by introduction of heavy atom with the aim of enhancing intersystem crossing and ROS-producing capacities, as well as a variety of targeting moieties for precise subcellular trafficking toward mitochondria, lysosomes and endoplasmic reticulum, respectively. Hence, upon selective translocalization of the proposed photosensitizers into organelles, the ROS converted from $^3O_2$ to $^1O_2$ can cause oxidative damage efficiently to the organelles. Interestingly, we found that the above-mentioned different subcellular target photosensitizers can cause cancer cells pyroptosis in varying degrees. More importantly, the occurrence of pyroptosis also stimulate ICD and facilitate the prime of immunity. Hence, the intriguing synergy of photodynamic therapy and immunotherapy for tumor treatment could be realized.

2. Experimental

2.1. Materials

DPBF and Reactive Oxygen Species Assay Kit (DCFH-DA) were obtained from Beyotime biotechnology Co., Ltd. Hoechst 33324, MitoTracker Green FM, and LysoTracker Green DND-26, were purchased from Thermo (invitrogen). ER-Tracker Green (BODIPY® FL Glibenclamide) was purchased from MKBio. The anti-CD11c-APC, anti-CD80-FITC, anti-CD86-PE-Cy5.5, anti-CD3-FITC, anti-FOXP3-PE, and anti-CD4-PE-Cyanine7 were purchased from BioLegend (San Diego, CA, USA).

2.2. Determination of singlet oxygen quantum yield (ϕΔ)

1,3-Diphenylisobenzofuran (DPBF) as a singlet oxygen indicator was added into sample solution (DCM) containing **Mito-ZS**, **Lyso-ZS** or **ER-ZS** (10 μM) to adjust the absorbance at 415 nm close to 1.0. Afterward, the mixed solution was treated with 580 nm laser irradiation (10 mW/

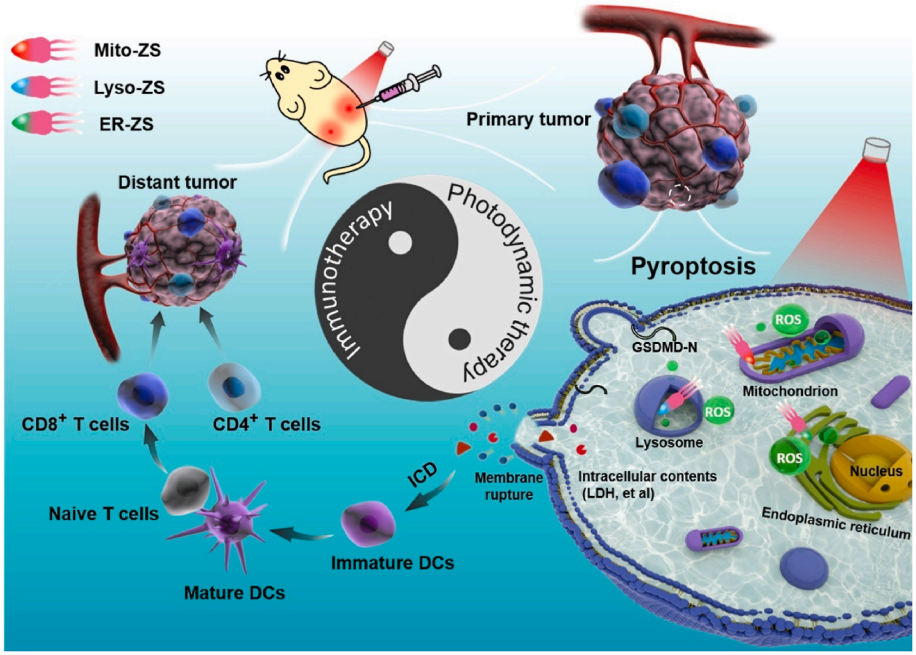

Scheme 1. Schematic diagram in illustrating molecular mechanism of **Mito-ZS**, **Lyso-ZS** and **ER-ZS** for anti-tumor therapy.

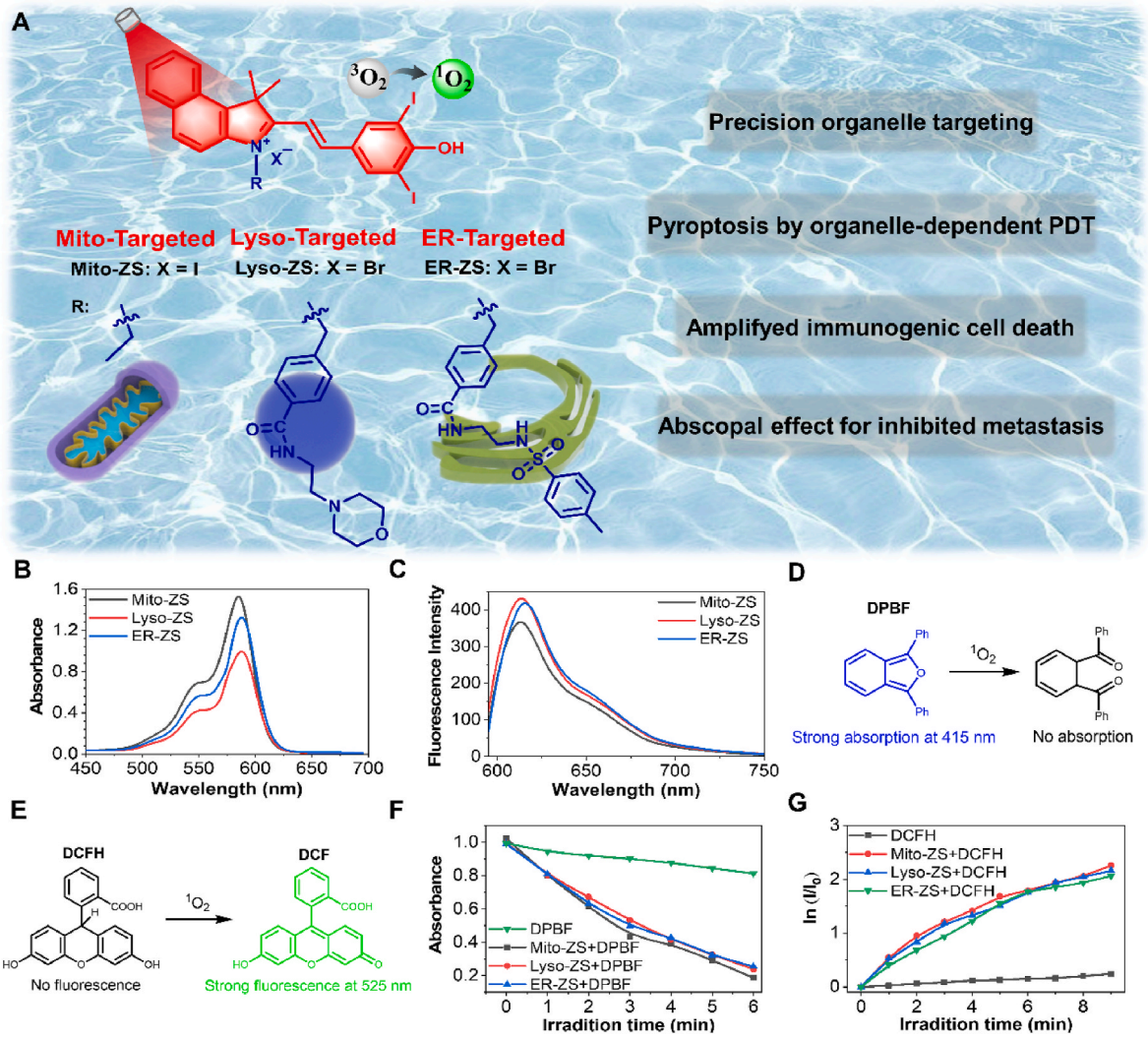

Fig. 1. (A) Schematic showing the different organelle-targeting photosensitizers. (B) Absorption and (C) fluorescence emission spectra of the photosensitizers with varied subcellular targeting motifs (10 μM, $\lambda_{ex} = 580$ nm). Schematic illustration of the mechanism of (D) DPBF and (E) DCFH for $^1O_2$ detection. (F) Quantification of the produced $^1O_2$ using DPBF as an indicator. (G) Quantification of the produced ROS using DCFH as an indicator, ln (I/I_0) as a function of excitation periods, where I_0 and I stand for fluorescence intensities of DCFH ($\lambda_{ex} = 488$ nm, $\lambda_{em} = 525$ nm) prior to and post excitation (10 mW/cm^2), respectively.

cm^2) for different time and the absorption spectra of DPBF were measured. The Rose Bengal (RB, 10 μM) was tested under the same experimental procedures as the reference (Fig. S13). At last, the singlet oxygen quantum yield was calculated with the following equation:

$$\varphi_{\Delta} = \varphi_{RB} \times (K_{Ps} \times F_{RB})/(K_{RB} \times F_{Ps})$$

ϕΔ represents the singlet oxygen quantum yield of the tested photosensitizer; ϕRB represents the singlet oxygen quantum yield of RB and the value is 0.76; Ps represents the tested photosensitizer; k represents the slope of the decrease of the absorbance at 415 nm of DPBF with the addition of irradiation time; F is the correction factor which is calculated by the following equation:

$$F = 1 - 10^{-OD}$$

OD represents the absorbance of the mixture at 580 nm.

2.3. Cell culture

The cancer cells (HeLa cells and 4T1 cells) were purchased from Institute of Basic Medical Sciences (IBMS) of the Chinese Academy of Science. The HeLa cells were cultured with DMEM high glucose medium and 4T1 cells were cultured with RPMI-1640 medium. These cancer cells were grown in the above medium containing 10% fetal bovine serum and 1% antibiotics (penicillin/streptomycin, 100 U mL^{-1}) at 37 °C in a humidified environment of 5% CO_2.

2.4. Intracellular tracking

HeLa and 4T1 cell lines were used for this study. The cells were incubated with fresh medium containing **Mito-ZS**, **Lyso-ZS** or **ER-ZS** (10 μM) for 20 min and washed with PBS, followed by costaining with 1 μM commercial dyes (Mito-Tracker Green, Lyso-Tracker Green and ER-Tracker Green) for 20 min. After that, the samples were washed with PBS and imaged by CLSM to investigate the subcellular localization of **Mito-ZS**, **Lyso-ZS** or **ER-ZS**. Conditions: excitation wavelength: 488 nm for Mito-Tracker Green, Lyso-Tracker Green, ER-Tracker Green and 580 nm for **Mito-ZS**, **Lyso-ZS** or **ER-ZS**; emission filter: 510–530 nm for Mito-Tracker Green, Lyso-Tracker Green, ER-Tracker Green and 600–700 nm for **Mito-ZS**, **Lyso-ZS** or **ER-ZS**. After fluorescence images were collected, the analysis was performed with Image J. software.

2.5. Intracellular ROS imaging

DCFH-DA was used to prove the generation of $^1O_2$ in 4T1 cells. 4T1

cells were plated onto 35 mmol confocal dishes and incubated with 5 μM **Mito-ZS**, **Lyso-ZS** or **ER-ZS** for 1 h, then staining with DCFH-DA (10 μM) for 30 min. After washed with serum free medium, the light group was irradiated with 580 nm LED light (40 mW, 5 min, 12 J/cm^2). Then confocal fluorescence imaging was carried out and collected. Conditions: excitation wavelength was 488 nm and emission wavelength was 500–530 nm for DCF.

2.6. LDH release assays

4T1 cells were plated at 1 × 10^5 cells per well in a 96-well cell-culture plate, followed by incubation at 37 °C for 24 h. Then the cells were incubated with 5 μM **Mito-ZS**, **Lyso-ZS** or **ER-ZS** for 1 h and washed with 100 μL fresh medium. The light groups were irradiated with 580 nm LED lamp at a power density of 40 mW/cm^2 for 10 min and continued growing for 12 h. The LDH release were detected according to the instruction manual.

2.7. In vitro cytotoxicity assays

4T1 cells were plated at 1 × 10^5 cells per well in a 96-well cell-culture plate, followed by incubation at 37 °C for 24 h. Then the cells were incubated with varying concentrations of different photosensitizers for 1 h and washed with 100 μL fresh medium. Then the cells were irradiated with 580 nm LED lamp at a power density of 40 mW/cm^2 for 10 min and continued growing for 12 h. The fresh medium (100 μL) and MTT (10 μL, 5 mg/mL) were added to each well and the cells were incubated for another 4 h at 37 °C. Finally, the absorbance of 560 nm was measured with a Bio-Rad microplate reader and the cell viability was calculated. For dark toxicity measurement of different photosensitizers, no light irradiation was applied to this experiment, and all other steps were the same.

2.8. Western blotting analysis

4T1 cells treated with different formulations (**Mito-ZS**, **Lyso-ZS** and **ER-ZS**) upon light irradiation or under dark were collected and subjected to standard Western blot analysis. Non-treated 4T1 cells were used as control. In brief, extracted proteins were separated by SDS-PAGE and then transferred to polyvinylidene difluoride (PVDF) membranes. The membranes were blocked with 5% nonfat milk solution to prevent the interference from non-specific binding and incubated with indicated primary antibody against GSDMD (Abcam Cambridge, MA, USA) and β-actin (Proteintech Group, Inc. Chicago, USA) overnight at 4 °C. After incubation with the goat-anti-rabbit IgG-HRP secondary antibody (Thermo Fisher scientific, Oregon, USA) at room temperature for 2 h, the immolunoreactive bands were determined using a chemiluminescence (ECL) system (Bio-Rad, CA, USA).

2.9. CRT staining in 4T1 cancer cells

4T1 cells were plated onto 35 mm confocal dishes and incubated with 5 μM **Mito-ZS**, **Lyso-ZS** or **ER-ZS** for 1 h, then the cells were washed and irradiated by 580 nm LED lamp irradiation (40 mW/cm^2) for 10 min. After 12 h, the cells were washed with pre-cooled 1 × PBS, fixed with 4% paraformaldehyde on the ice for 1 min, and further incubated with ATTO 488 labelled CRT antibody for 1 h. The CRT expression fluorescence images collected by CLSM with the excitation at 488 nm and signal acquisition in the range from 500 to 540 nm.

2.10. Antitumor capacity in vivo

The 4–6 weeks old BALB/c mice were chosen and 4T1 tumors were established by s. c. injecting 2 × 10^6 4T1 cells. When the primary tumor volume reached 150 mm^3, the tumor-bearing mice were randomly divided into seven groups (PBS, **Mito-ZS**, **Lyso-ZS**, **ER-ZS**, **Mito-ZS** + Light, **Lyso-ZS** + Light and **ER-ZS** + Light, n = 5). The light group were irradiated with 580 nm laser for 20 min at photodensity of 100 mW/cm^2. The distant tumor was established by s.c. injecting 1 × 10^5 4T1 cells at 3 days after the treatment. As for live-imaging, the mice injected with 50 μM (100 μL) different photosensitizers and imaged with a NightOWL II LB983 small animal *in vivo* imaging system. The fluorescence was excited at 580 nm and collected at 650 ± 20 nm. The tumor volume was calculated by using the formula:

$$v = \frac{1}{2} \times a \times b^2$$

V represents the tumor volume of mice, a represents the longest diameter of the tumor region, and b represents the diameter in the vertical direction according to a of the tumor region. All the animal experiments involved in this study were conducted in accordance with the Guide for the Care and Use of Laboratory Animals published by the US National Institutes of Health (8th edition, 2011), and approved by the local research ethics review board of the Animal Ethics Commolittee of Dalian University of Technology.

2.11. Anti-metastasis effect

The primary tumors were established and treated with different formulations as the methods described previously. When the primary tumor treated with different treatment, the 2 × 10^6 4T1 cells were administered intravenously via tail vein infusion into each BALB/c mouse. 7 d later, after sacrificed mice, the lungs were photographed, while the spleens were taken out for testing proportions of memory T cells by flow cytometry.

3. Results and discussion

3.1. Preparation and characterization of organelle-targeting photosensitizers

The scheme of proposed photosensitizers was shown in Fig. 1A, the synthetic routes were summarized in Fig. S1 and all the intermediates and the ultimate products were confirmed by ^{1}H NMR, ^{13}C NMR, and HRMS (Figs. S2–S12). Overall, UV–Vis absorption analysis revealed similar spectra of the yielded photosensitizers, characterized to exhibit strong absorption at 580 nm assignable to the cyanine moiety (Fig. 1B). On the other hand, under excitation at 580 nm, tissue-penetrating emission (600–750 nm, maximal: 620 nm) was determined (Fig. 1C) and implied their potentials in self-tracking and theranostic utilities. Quantitative measurements on $^1O_2$ production based on DPBF (Fig. 1D) and DCFH (Fig. 1E) assays approved their comparable ROS-producing capacities upon excitation at 580 nm (Fig. 1F and G), the singlet oxygen quantum yield (compared with rose bengal) was calculated to be approximately 5.16%, 5.44% and 5.17% for **Mito-ZS**, **Lyso-ZS** and **ER-ZS**, respectively (Fig. S13), which is assumed to be straightforward in exploring the impact of organelle-dependent PDT on the cell death paradigms.

3.2. Intracellular tracking and intracellular ROS imaging

To validate the subcellular organelle-targeting functionalities of our elaborated photosensitizers, their intracellular distributions were investigated by Confocal Laser Scanning Microscopy (CLSM). Note that a class of commercial dyes, including Mito-Tracker®, Lyso-Tracker® and ER-Tracker®, were employed for prior labelling the intended subcellular compartments of mitochondria, lysosomes and endoplasmic reticulum, respectively. As shown in Fig. 2A, excellent target accumulation into the distinctive organelles was accomplished by all three photosensitizers, as supported by high-degree colocalizations of the photosensitizers (red) and the commercial organelle-staining dyes (green). The colocalization coefficients were calculated to be approximately 0.96 (mitochondria),

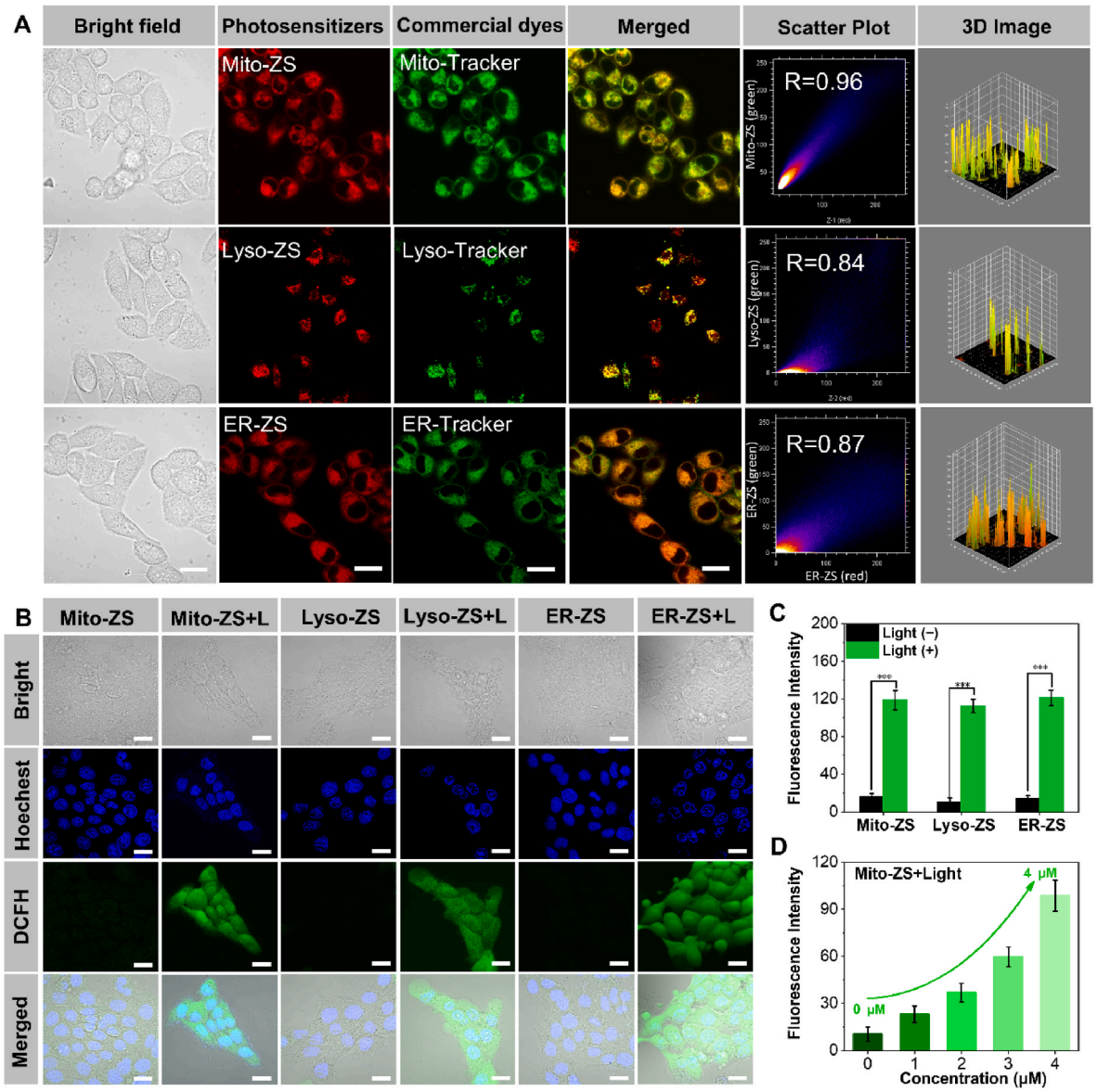

Fig. 2. (A) Intracellular distributions of **Mito-ZS**, **Lyso-ZS** and **ER-ZS** (red, λ_{ex} = 580 nm, λ_{em} = 600–700 nm) by CLSM observation, wherein mitochondria, lysosomes and endoplasmic reticulum were stained by commercial dyes (λ_{ex} = 488 nm, λ_{em} = 510–530 nm) of Mito-Tracker Green, Lyso-Tracker Green or ER-Tracker Green, respectively. Scale bars: 20 μm. (B) ROS detection in 4T1 cells using DCFH-DA as the fluorescence indicator. Blue fluorescence (λ_{ex} = 405 nm, λ_{em} = 450–470 nm); green fluorescence (λex = 488 nm, λem = 510–530 nm). Scale bars: 20 μm. (C) The quantified fluorescence intensities of DCFH-DA. (D) Fluorescence intensities of DCFH-DA as a function of **Mito-ZS** concentration upon excitation at 580 nm (40 mW/cm^2, 5 min, 12 J/cm^2).

0.84 (lysosomes) and 0.87 (endoplasmic reticulum) (Table 1), respectively. Notably, **Mito-ZS** owing to its cationic charge and appropriate lipophilicity enables target transportation to the mitochondria in light of the remarkably negative charge of mitochondrial membranes (~−220 mV) in cancerous cells [35,36]. Furthermore, our proposed photosensitizers were determined to persistently reside in the targeted organelles despite extended incubation (4 h, Fig. S14). These appreciably high colocalization coefficients authenticate the validity of our molecular design in pursuit of targeted accumulation at the distinct organelles.

Furthermore, intracellular ROS production was studied with the aid of ROS reporter (2,7-dichlorodihydrofluorescin diacetate: DCFH-DA), wherein non-fluorescent DCFH-DA could be converted to be fluorescent emissive DCF due to its reaction with ROS. Pertaining to 4T1 cells incubated in presence of the proposed three photosensitizers, bright fluorescence (green) was uniformly observed in the cell interiors under excitation at 580 nm (12 J/cm^2, Fig. 2B and C). Moreover, quantitative measurement verified consistent rise in ROS production along the rising dosages of photosensitizers (Fig. 2D and Fig. S15). Nonetheless, the

Table 1
The colocalization coefficients of photosensitizers and commercial organelle-staining dyes.

Photosensitizers	Targeting moities	Targeting organelles	Commercial dyes	Colocalization degree
Mito-ZS	Indolyl cation	Mitochondria	Mito-Tracker®	0.96
Lyso-ZS	Morpholine group	Lysosomes	Lyso-Tracker®	0.84
ER-ZS	Methylbenzenesulfonamide	Endoplasmic reticulum	ER-Tracker®	0.87

overall ROS production was determined to be fairly comparable for the proposed three photosensitizers if an equal dosage or excitation period was applied, of particular convenience to interrogate the impact of organelle-dependent PDT on the cytocidal pathway. The cytotoxic consequence of the produced ROS aiming at the vital subcellular compartments were assessed based on Calcein-AM (liver cells, green) and PI (dead cells, red) assay. Overwhelming cytotoxic potencies were concluded for our proposed organelle-targeting PDT. Cell nuclei were observed to be uniformly stained into red upon PDT as opposed to negligible dark cytotoxicity (Fig. S16).

3.3. *In vitro phototoxicity and morphological of pyroptosis*

Furthermore, the cellular morphologic changes post precise organelle-targeted PDT (580 nm, 24 J/cm^2) were recorded based on real-time CLSM observation, wherein the cells were incubated in Confocal Chamber at 37 °C supplemented with 5% CO_2. As shown in Fig. 3A, bubble-like protrusions (indicated by white arrows in Fig. 3A) from plasma membrane, in reminiscence of blebs, could be clearly identified for the cells upon treatment of **Mito-ZS**, **Lyso-ZS** and **ER-ZS** under excitation at 580 nm (24 J/cm^2) despite the varied occurrence rates. Moreover, real-time CLSM observation witnessed progressively inflating bubbles (Supplementary Video S1). Note that these bubble-like protrusions closely resemble pyroptotic bodies, a unique characteristic of pyroptosis [8,9], manifesting that organelle targeting of PDT may lead to the occurrence of pyroptosis. With the intention of ruling out that the bubbles as a result of apoptosis, we used H_2O_2 as a classical apoptosis inducer as a control. As shown in Fig. 3B, as opposed to abundant bubbles by our proposed subcellular organelle-targeted PDT (**Mito-ZS** + L and **ER-ZS** + L), very limited bubbles could be observed upon H_2O_2 treatment. Moreover, the appearances of the bubbles are significantly different. The size of the bubbles produced by H_2O_2-induced apoptosis is very small and does not change significantly over time. However, the bubbles generated by **Mito-ZS** + L and **ER-ZS** + L expand rapidly in a short period of time until the cell membrane ruptures to fully release the intracellular material.

Supplementary data related to this article can be found at https://doi.org/10.1016/j.bioactmat.2022.07.016.

Another distinguished characteristic of pyroptosis is the improved permeabilities of plasma membrane for mass transportation between intracellular and extracellular compartments. To assess the cytoplasmic permeabilities, cytomembrane impermeable dyes of annexin V (AV, green) and propidium iodide (PI, red) were employed due to their selective affinities to phosphatidylserine (located on the inner cytoplasmic surface of plasma membrane) and nuclei, respectively. As shown in Fig. 3B, simultaneous positive staining of both cytoplasmic phosphatidylserine and nuclei could be observed for 4T1 cells upon PDT, as opposed to the classical apoptosis induced by H_2O_2 wherein positive AV-

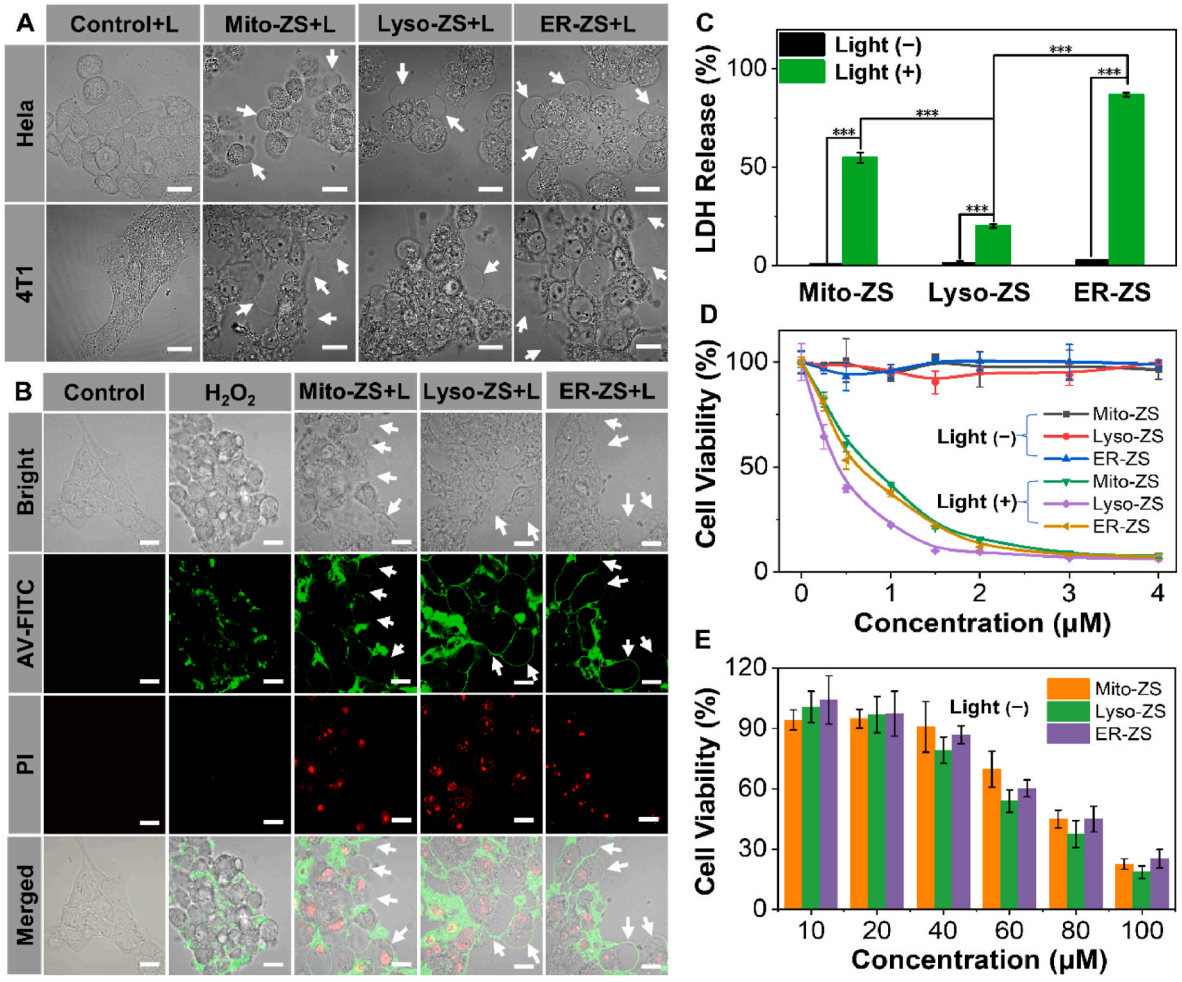

Fig. 3. (A) Representative morphologies of HeLa and 4T1 cells under treatment of diverse organelle-targeting photosensitizers (5 μM) in presence or absence of excitation (580 nm, 40 mW/cm^2, 10 min, 24 J/cm^2). Scale bars: 20 μm. (B) Annexin V-FITC/PI co-staining assay, red fluorescence of PI (λ_{ex} = 488 nm, λ_{em} = 650–750 nm) and green fluorescence of Annexin V (λ_{ex} = 488 nm, λ_{em} = 510–530 nm). Scale bars: 20 μm. (C) Quantification of LDH release. (D) Cell viabilities of 4T1 cells under treatment of diverse organelletargeting photosensitizers (0–4 μM) in presence or absence of excitation (580 nm, 40 mW/cm^2, 10 min, 24 J/cm^2). (E) Dark cytotoxicities of a variety of organelle-targeting photosensitizers against 4T1 cells. (*$p < 0.05$, **$p < 0.01$, ***$p < 0.001$.)

staining could be only observed due to preserved cytoplasmic integrity and partial translocation of phosphatidylserine to extracellular leaflet during apoptosis. Moreover, bubble-like protrusions appeared to be perfectly stained by AV as uniform and continued circle lines, as opposed to the clustered AV-positive domains on the plasma membranes under treatment of H_2O_2. This contrasting observation again indicated organelle-targeting PDT in stimulating pyroptosis rather than apoptosis.

The loss of plasma membrane integrity due to pyroptosis permits passive migration of AV and PI through plasma membrane to access their intracellular targets, which apparently could also prompt the leakage of intracellular components to the extracellular compartments. Herein, lactate dehydrogenase (LDH) was utilized as the model molecule to estimate the leakage of intracellular contents for 4T1 cells upon PDT from **Mito-ZS**, **Lyso-ZS** and **ER-ZS**. In consistent with our speculation, as opposed to negligible LDH leakage under dark, substantial LDH was determined to release into the extracellular compartments, **Lyso-ZS** (20.1%), **Mito-ZS** (54.7%), **ER-ZS** (86.8%) (Fig. 3C). Basically, the occurrence rates of the bubble-like protrusions seemed to be well correlated with the levels of LDH leakage. Hence, in view of their comparable ROS production, localized photochemical reactions in distinctive organelles are speculated to result in diversified cell death paradigms. Possibly, pyroptosis was most favorably stimulated by ER-targeted PDT from **ER-ZS**, yet pyroptotic rates was speculated to be lowest for Lyso-targeted PDT from **Lyso-ZS**.

To our interest, MTT assay (Fig. 3D) on cell viabilities upon PDT revealed contrasting tendencies, wherein highest light cytotoxic potencies were actually accomplished by **Lyso-ZS** (IC_{50}: 0.42 μM) rather than comparably lowered cytotoxic potencies of **Mito-ZS** (IC_{50}: 0.78 μM) and **ER-ZS** (IC_{50}: 0.43 μM). And the IC_{50} indexes in dark of **Mito-ZS**, **Lyso-ZS** and **ER-ZS** respectively were calculated to be approximately 79.46 μM, 80.43 μM and 86.15 μM, respectively, which is hundredfold less toxic than their phototoxicities. (Fig. 3E). This inconsistency of light cytotoxic again suggests distinguished cell death paradigms for our proposed varied subcellular targeting photosensitizers. Most likely, the major pyroptotic pathways induced by **Mito-ZS** and **ER-ZS** is characterized by bubble-like protrusions, yet the major apoptotic pathway (despite relatively low rate of pyroptotic occurrence) by **Lyso-ZS** preventing leakage of intracellular contents. Therefore, pyroptosis may not quantitatively upgrade the direct lethal potencies to the affected cells but the most rewarding advantage of pyroptosis lies in its capacities in prompting cell immunogenic death, which potentially facilitates the development of anti-tumor immunities in subsequent suppression of the primary tumors and distant metastasis through abscopal effect. Hence, we aspire to explore deep insights into the immunostimulatory effects by a variety of organelle targeting PDT in the subsequent experiments.

3.4. Mechanism analysis of organelle-targeting photosensitizers initiated pyroptosis

To explore detailed insights into the genetic variables involved in organelle-targeted PDT, transcriptomics study was conducted by comprehensive RNA-seq analysis with the intention of scrutinizing the impact of PDT on the transcriptional map. Meanwhile, differential analysis was conducted by using Ingenuity Pathway Analysis (IPA) with

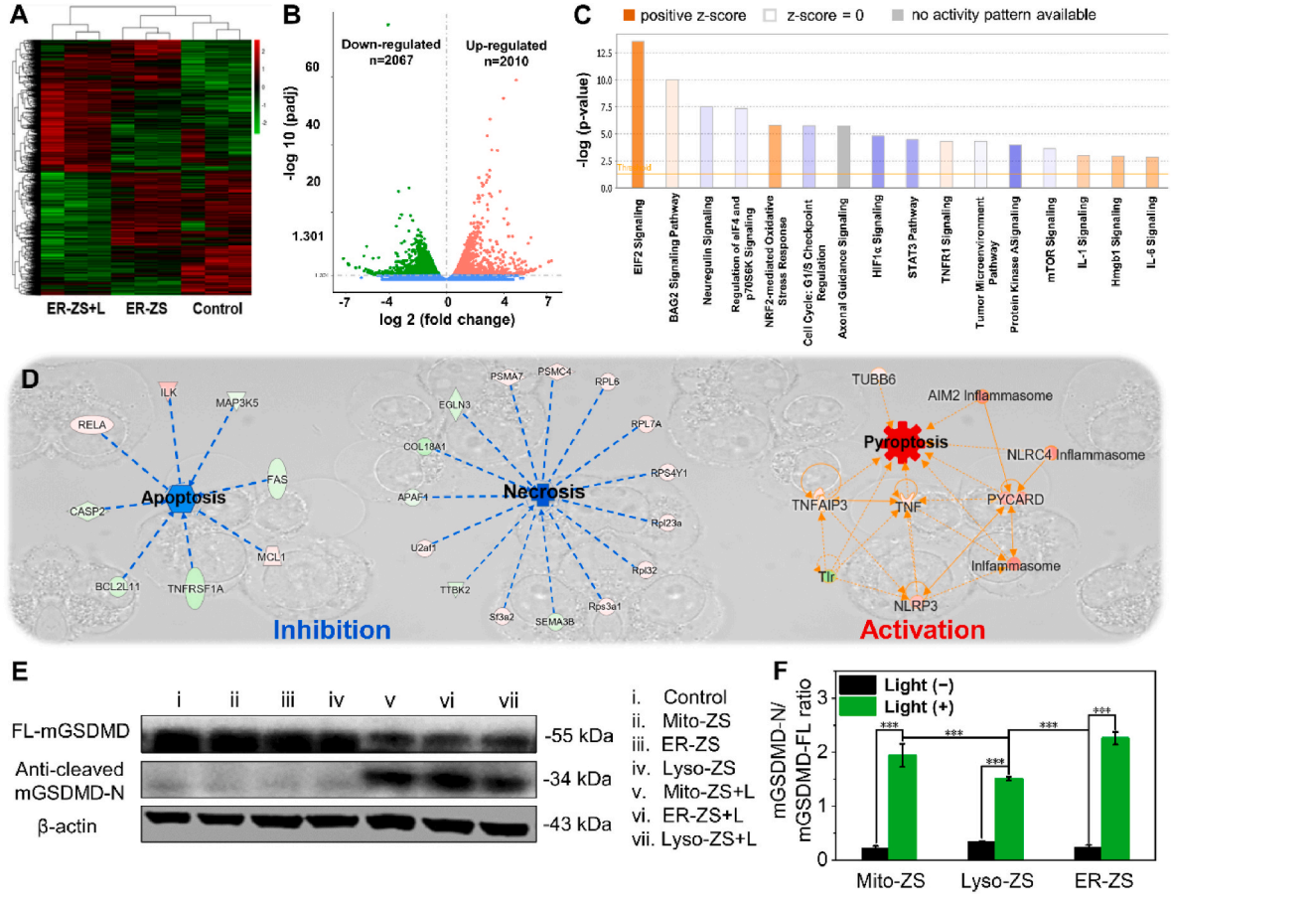

Fig. 4. (A) Heat map in pertinent to transcriptomics of 4T1 cells prior to and post PDT. (B) Volcano plot of **ER-ZS** + L vs control. Control group is normal 4T1 cells. (C) Impact of PDT on a number of important signaling pathways based on IPA analysis. (D) Pyroptosis pathway was activated upon PDT based on transcriptomic analysis. (E) Western blot for identification of the liberation of gasdermins in 4T1 cells under treatment with the diverse organelle-targeting photosensitizers (5 μM) in presence or absence of excitation (580 nm, 40 mW/cm^2, 10 min, 24 J/cm^2). (F) The ratio of mGSDMD-N to mGSDMD-FL were statistically analyzed. (*$p < 0.05$, **$p < 0.01$, ***$p < 0.001$.)

the aim of unveiling the molecular signalling pathways in pertinent to PDT. Overall, in relative to the blank control, 2010 genes were subjected to upregulation and 2067 genes were downregulated upon PDT (Fig. 4A and B). In reference to gene ontology, the main differences in the biological processes of 4T1 cells prior to and post PDT is involved in biomolecule metabolic processes, including ribosome, rRNA metabolism, nucleolar and preribosome, etc. (Fig. S17). In addition, the Kyoto Encyclopedia of Genes and Genomes (KEGG) pathway enrichment analysis of differentially expressed genes was performed (Fig. S18). The pathways of ribosome biogenesis in eukaryotes, RNA transport, and spliceosome, etc. were demonstrated to be upregulated by the differentially expressed genes. Also, a variety of ROS-associated genes, including TRPV1, XBP1, TNF, IL6 and BAX, were upregulated (Fig. S19). In particular, endoplasmic reticulum stress was indicated with respect to the activated EIF_2 signaling pathway (Fig. 4C), in agreement with our strategically precision PDT at endoplasmic reticulum. Leadingly, antioxidant machinery of NRF2 responsible for eliminating the produced ROS was also observed to be activated. To discriminate the cell death paradigms, differential analysis was emphasized on the signaling pathways in pertinent to apoptosis, necrosis and pyroptosis. As shown in Fig. 4D, apoptotic and necrotic pathways appeared to be relatively inhibited, yet pyroptosis was significantly activated upon PDT. Given that the pioneer researches implied the correlation of ROS with activation of NLRP3 inflammasomes [30], our transcriptomics investigations obtained consistent results that substantial upregulated NLRP3 was initiated in response to PDT. In addition, another two important pro-pyroptotic inflammasones (AIM2 and NLRC4 reported to be involved in double-stranded DNA damage and microbes pyoptosis [37, 38], respectively) appeared to be also upregulated. This interesting observation implied the possibilities of our proposed organelle-targeting PDT could potentially instigate a variety of molecular pathways towards pyroptosis. The formation of these pro-pyroptotic inflammasomes was supported in view of the upregulated PYCARD (encoding the essential inflammasome adaptor-protein ASC, thereby engaged in assembly of NLRP3 inflammasomes). Furthermore, with aids of a number of upregulated co-factors (*e.g.,* TNF, TNFAIP3, TUBB6, Fig. 4D), the aforementioned pro-pyroptotic inflammasomes could urge activation of pyroptosis-specific caspases and commitment of hydrolysis and liberation of pore-forming gasdermins for the rupture of plasma membranes. The liberation of pore-forming gasdermins (GSDMD-N) were indeed confirmed by Western blot analysis (Fig. 4E and F). GSDMD-N were determined to be significantly higher for the cells upon PDT treatment, approving the liberation of pyroptotic trademark gasdermins for eliciting the subsequent pore-forming and rupture of plasma membranes.

To further verify the advantages of organelle-targeted photosensitizers in regulating pyroptosis, non-organelle-targeted commercial photosensitizer of Ce6 was selected as a control for insight into the level of GSDMD and caspase-1 by Western blot analysis. As shown in Fig. S20, the levels of the activated caspase-1 and GSDMD in the cells upon treatment with our proposed organelle-targeted photosensitizers were determined to be significantly higher than those of Ce6, indicating the worthy of our precise organelle-targeted PDT strategy in pursuit of maximized degrees of pyroptosis, especially targeting mitochondria and endoplasmic reticulum.

In summary, according to the results of RNA-seq and Western blot analysis, once the **Mito-ZS**, **Lyso-ZS** and **ER-ZS** accumulated into the distinct subcellular organelles, the localized PDT in differing organelles was determined to lead to contrasting degrees in stimulating NLRP3, thus accounting for varied degrees in activation of caspase 1, followed by cleavage of GSDMD into GSDME-N fragment for perforating cytomembranes and pyroptosis (Fig. S21). Eventually, the immunostimulatory intracellular components [*e.g.,* lactate dehydrogenase (LDH) and inflammatory cytokines] could outflux through the ruptured plasma membranes and prompt strong inflammatory response for development of ICD.

3.5. ICD effect induced by pyroptosis

One of most intriguing aspects of pyroptosis for anti-tumor therapy is its potentials in instigating overwhelming anti-tumor immunities, which is stimulated as a consequence of not only the aforementioned release of intracellular pro-inflammatory components but also presentation of damage associated molecular patterns (DAMPs) on the cytoplasmic surface [39–41]. In particular, pioneer researches revealed that translocation of calreticulin (CRT) from intracellular endoplasmic reticulum compartments to the external surface of cytomembrane and ATP released were crucial in pyroptosis with the aim of activation of ICD and the ensuing DCs' maturation and immunity [42–46]. Our subsequent immunostaining assay pertaining to CRT identified abundant translocation of CRT onto the cytoplamsic surface of the cells upon PDT treatment by **Mito-ZS** and **ER-ZS** (Fig. 5A and C), in contrast to markedly low cytoplasmic CRT for **Lyso-ZS**-treated cells. In addition, as shown in Fig. S22, compared to Ce6-treated cells, the Western blot results also proved that photosensitizers with organelle targeting enable promoted CRT translocation, thus accounting for significantly more pronounced ICD effect. And the result of ATP released in the cell supernatants also has a similar trend with the CRT immunostaining assay (Fig. 5D), wherein the leakage levels of ATP was significantly higher in **Mito-ZS** + L and **ER-ZS** + L treated groups in relative to that of **Lyso-ZS** + L treated group.

To further verify that the importance of pyroptosis in augmenting the immunogenic potentials, the DCs' maturation characterized to possess positive CD80 and CD86 was evaluated by Flow Cytometry. In accordance to our speculation, the prompted DCs' maturation (Fig. 5B and Fig. S23) was confirmed for bone marrow dendritic cells (BMDCs from Balb/c mice) that were subjected to co-incubation with 4T1 cells upon PDT. Moreover, interleukin 12 (IL-12p70), interleukin 6 (IL-6), tumor necrosis factor α (TNF-α) and interleukin 4 (IL-4), correlated to activation of DCs and T lymphocytes and development of both innate and specific immunities, were measured by enzyme-linked immune sorbent assay (ELISA) to be significantly higher for the cells under PDT by **Mito-ZS** and **ER-ZS** rather **Lyso-ZS** (Fig. 5E–H).

To further verify that the immunostimulatory effect was caused by pyroptosis rather than necrosis, the Western blot analysis was performed for insight into the necrosis marker protein P-MLKL post PDT treatment. Herein, Necroptosis Inducer Kit of TSZ was included as a positive control for necrosis. As shown in Fig. S24, as opposed to the positive control of TSZ in stimulating necrosis (augmented level of P-MLKL), the negligible level of P-MLKL was confirmed for the cells despite PDT treatment, indicating unlikeliness of necrotic pathway in pertinent to PDT-stimulated cell death. This result further confirmed that the immunostimulatory effect should be as a consequence of pyroptosis. Hence, the obtained results verified the importance of targeted PDT at the mitochondria or endoplasmic reticulum compartments in pursuit of pyroptosis, which accordingly faciliate acquirement of stimulated immunities for propogated clearance of pathogens (*e.g.,* tumors).

3.6. In vivo antitumor activity

Eventually, we attempted to implement pyroptosis by organelle-targeting PDT for treatment of intractable triple-negative breast cancer. Prior to *in vivo* investigations, the pyroptotic potencies were assessed based on a classical cell scratch assay, and the subsequent results identified rapid and potent cytocidal efficacy of our proposed organelle-targeting PDT (Fig. S25). Furthermore, organelle-targeting PDT was prescribed in treatment of not only the primary solid tumors via direct intratumor administration to explore the potencies of pyroptosis in eradication of primary tumors but also the distant tumors to inspect the feasibilities of pyroptosis in development of anti-tumor immunities for inhibiting tumor metastasis and recurrence. The therapeutic scheme was illustrated in Fig. 6A (note that spatiotemporal excitation was conducted at 2 h post intratumoral injection of

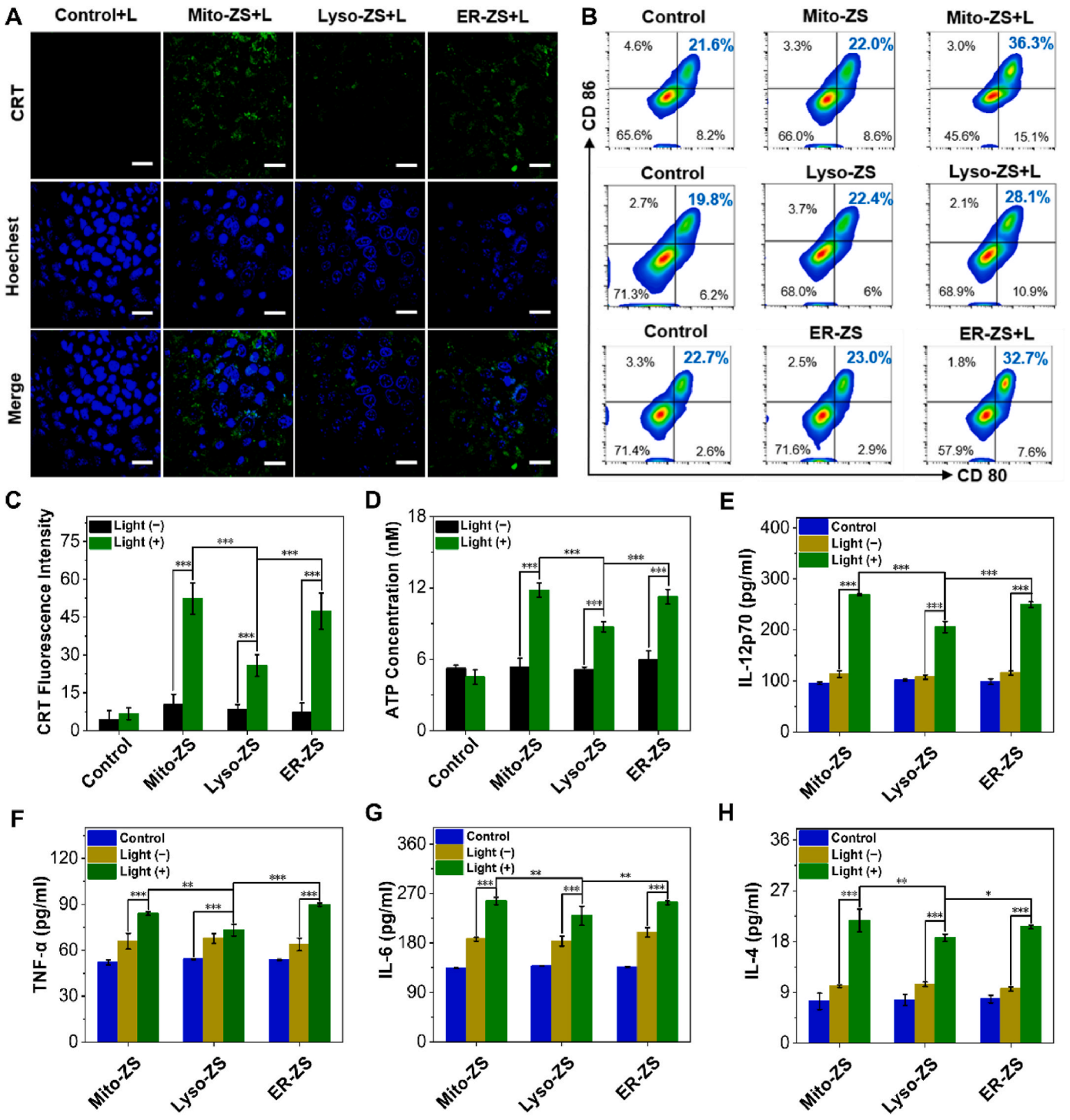

Fig. 5. (A) Identification of translocation of CRT to plasma membrane by CLSM. Scale bars: 20 μm. (B) Quantification of CD80 and CD86 by flow cytometry. (C) Quantified fluorescence intensities of CRT based on the representative CLSM images in (A). (D) Quantification of the extracellular levels of ATP for 4T1 cells upon PDT. (E–H) Quantification of the Secretion of IL-12p70, IL-6, TNF-α and IL-4 by ELISA assay (n = 3). The error bars (n = 3) represent means ± SD. (*$p < 0.05$, **$p < 0.01$, ***$p < 0.001$.) The 4T1 cells under treatment with the diverse organelle-targeting photosensitizers (5 μM) in presence or absence of excitation (580 nm, 40 mW/cm^2, 10 min, 24 J/cm^2).

photosensitizers based on the results in Fig. 6B).

Overall, the primary tumor growth of the intractable triple-negative 4T1 carcinoma appeared to be completely suppressed by PDT (Fig. 6C), verifying the overwhelming potencies of organelle-targeting PDT for pyroptosis and eradication of the solid tumors. To our interest, the tumor progression at the distant sites appeared to be substantially retarded for the mice whose primary tumors were subjected to PDT by **ER-ZS** and **Mito-ZS** (Fig. 6D), which should be accredited to superior anti-tumor immunities due to high-degree pyroptosis from treatment of **ER-ZS** and **Mito-ZS**. Indeed, the stimulated immune responses were confirmed by immunostaining the tumors upon PDT (Fig. 6F), wherein abundant CD11b$^+$, CD11c$^+$ dendritic cells for activation of specific anti-tumor immunity, as well as CD4$^+$, CD8$^+$ T lymphocytes for execution of specific anti-tumor immunity, were observed to infiltrate throughout the

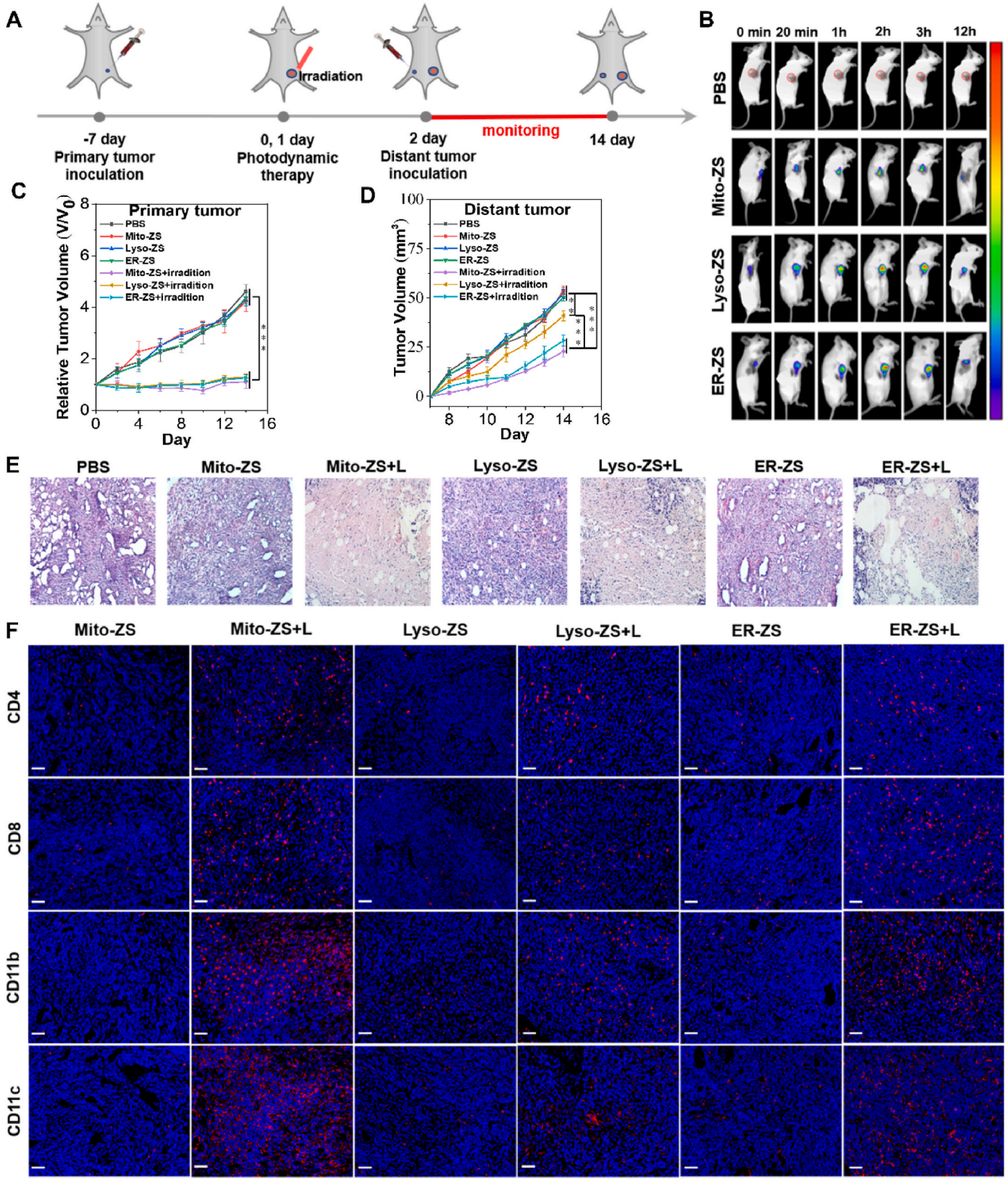

Fig. 6. (A) Diagrammatic illustration of the therapeutic scheme in treatment of primary tumors and distant tumors. (B) Biodistributions by IVIS. (C) Relative tumor growth profiles of the primary tumors upon PDT through intratumor dosage of photosensitizers. (D) Relative tumor growth profiles of the distant tumors upon intratumor dosage at the primary tumors. (E) H&E staining of the primary tumors on day 14 post diverse treatments. (F) Immunofluorescence staining for identification of $CD4^+$, $CD8^+$ T lymphocytes, and $CD11b^+$, $CD11c^+$ dendritic cells in the primary tumors post diverse treatments. Scale bars: 50 μm. (*$p < 0.05$, **$p < 0.01$, ***$p < 0.001$.)

tumors.

3.7. In vivo antitumor immunity

To further verify the immune effect induced by tumor pyroptosis *in vivo*, DCs maturation was further evaluated through flow cytometry analysis. Similar to the results of *in vitro*, the groups of **Mito-ZS** + L and **ER-ZS** + L had a significant DCs maturation rate (Fig. 7A and Fig. S26), which was also conducive to activating $CD8^+$ T cells to directly kill tumor cells and exert anti-tumor effects. As shown in Fig. 7B–E and Figs. S27–31, the populations of $CD4^+$, $CD8^+$ T cells and regulatory T cells (Tregs) in primary and distant tumors were determined. Note that the regulatory T cells interferes with the function of effector T cells and DCs, thereby inhibiting the anti-tumor immune effect [47]. Compared with the control group, the percentages of $CD8^+$ and $CD4^+$ T cells increased and Tregs decreased in the all PDT groups, especially in the groups of **Mito-ZS** + L and **ER-ZS** + L, the ratio of $CD8^+$/Treg cells reached the highest, it affirmed that oxidative stress at mitochondria and endoplasmic reticulum compartments appeared to prompt higher degree pyroptosis and significantly enhances specific anti-tumor

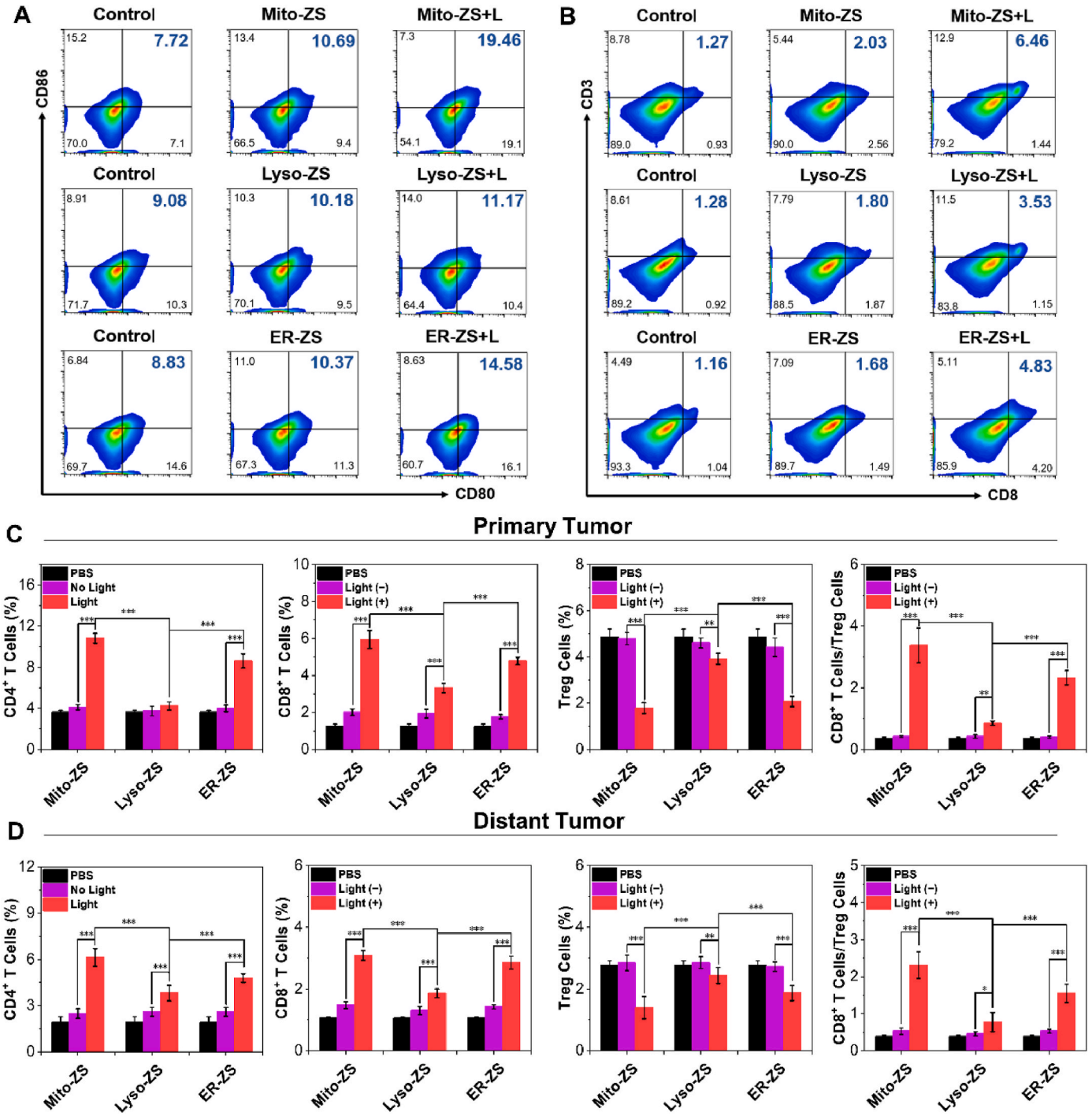

Fig. 7. Representative flow cytometry results (A) for estimation of mature DC cells and (B) $CD8^+$ T cells in primary tumors. Quantification of the percentages of $CD4^+$ T cells, $CD8^+$ T cells, Treg cells and the ratio of $CD8^+$ T cells/Treg cells based on Flow Cytometry for the cells from primary tumors (C) and distant tumors (D). The error bars (n = 5) represent means ± SD. $*p < 0.05$, $**p < 0.01$, $***p < 0.001$. 1×10^5 cells from the tumor were measured for each sample.

immunity.

The stimulated specific anti-tumor immunities are believed to conclude the observed anti-tumor potency for both primary tumors and distinct metastasis. Meanwhile, the body weight of all groups (Fig. S32) and histological analysis (Fig. 7E and Fig. S33) revealed the excellent safety profiles of spatiotemporal PDT by observation of no obvious morphological or histopathological abnormalities in other organs, but massive tumor cell death in primary tumor under PDT treatment was observed, indicating tumoral pyroptosis for targeted anti-tumor immunities in clearance of the pathologic tumors rather than non-specifically inflammatory reactions. Given the obviously immune effects of primary and distant tumors therapy, it has been hypothesized that immune memory effect would be augmented to prevent tumor recurrence and metastasis. The therapeutic scheme of lung metastasis was illustrated in Fig. 8A. To assess the immune memory effect, after 7 days of treatment, the spleens were taken out from the mice with primary tumor for testing proportions of memory T cells by flow cytometry. As shown in Fig. 8B–E, Figs. S34 and S35, the percentages of central memory T cells (TCM) and effector memory T cells (TEM) in mice treated with **Mito-ZS** + L and **ER-ZS** + L were significantly higher than the other groups. Furthermore, the immune memory effect was also confirmed in the pulmonary metastasis model, which was established in primary tumor mice by intravenous injection of 4T1 cells after different treatment. As displayed in photographs of lungs (Fig. 8F), compared with the control and no light group, there were no metastatic nodules in the lung tissues of mice in the normal, **Mito-ZS** + L and **ER-ZS** + L group. These results fully confirmed that **Mito-ZS** + L and **ER-ZS** + L could prim the immune memory effect of mice, thereby inhibiting tumor regeneration and metastasis.

4. Conclusions

In summary, we report the precise elaboration of a class of well-defined photosensitizers with excellent subcellular organelle-targeting function and in situ photochemistry organelles for varied degree pyroptosis towards the affected tumor cells. The pyroptotic rates were observed to follow a distinct organelle-targeting PDT-dependent manner, wherein the oxidative stress at mitochondria and endoplasmic reticulum compartments appeared to prompt higher degree pyroptosis. Of note, the prompted pyroptosis not only supported by the morphological and mechanistic characteristics but also for the first time fully validated by the subsequent comprehensive RNA-Seq analysis. Moreover, pyroptosis was delineated to promote the development of potent anti-tumor immunities as a result of uncontrolled release of intracellular immunostimulatory components and specifically presentation of DAMP on the cytoplasmic surface, eventually facilitating both innate anti-tumor immunities and maturation of DCs, T lymphocytes and memory T cells for specific anti-immunities maturation. The immunostimulatory capacities of pyroptosis eventually demonstrated to be favorable in situ eradication of the primary tumors but also propel clearance of distant tumors and metastatic tumors, advocating the worthy of our endeavors in pursuit of pyroptotic death pathway for potent anti-tumor therapy, particularly in elimination of metastasis and inhibition of tumor recurrence. To our best knowledge, our study could represent the first example of spatiotemporal PDT in accomplishing pyroptosis, what is more, for the first time reporting the importance of precisely subcellular organelle-targeted PDT in seeking maximized pyroptosis. Hence, the present study provides critical information in understanding the correlation of PDT and cytocidal pathways, which should be highlighted in

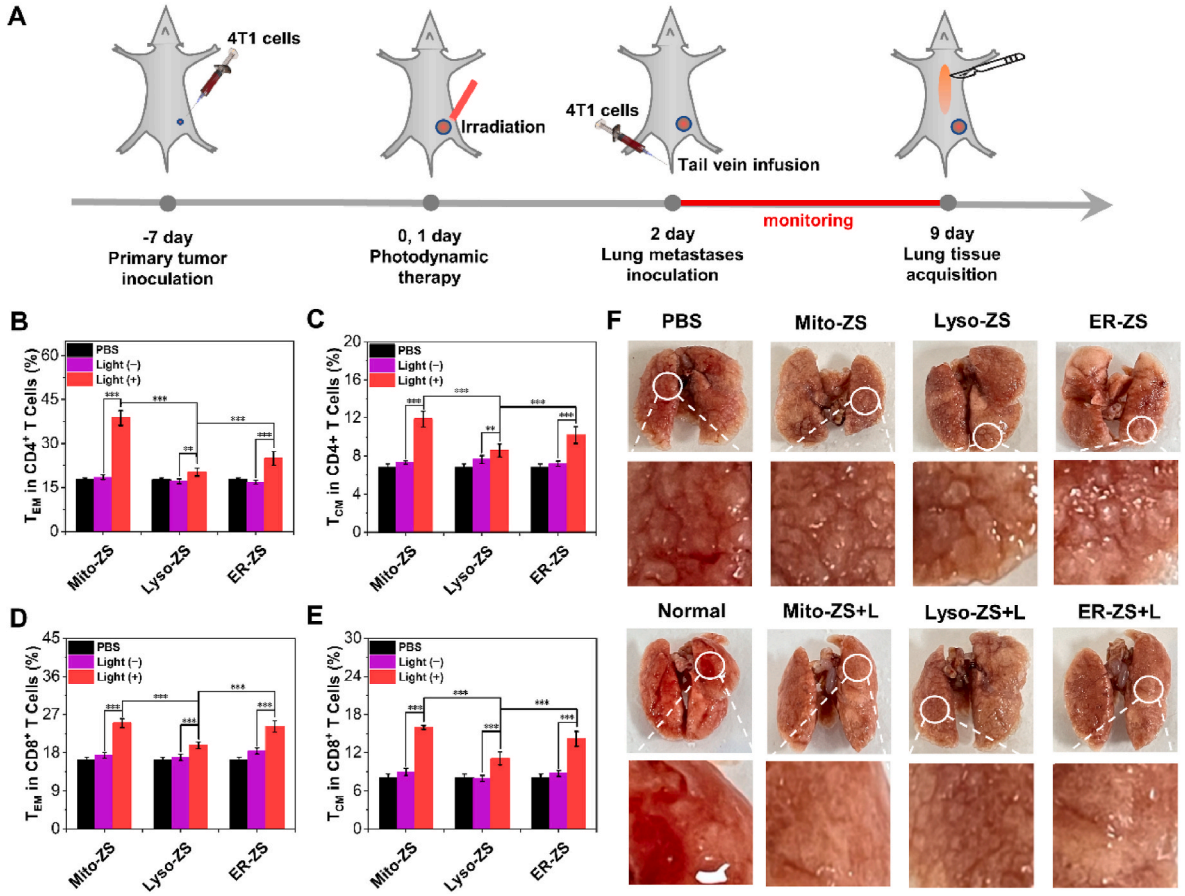

Fig. 8. (A) Diagrammatic illustration of the therapeutic scheme in treatment of primary tumors and pulmonary metastases. (B, C) Quantification of the $CD4^+$ effector memory T cells (B) and $CD4^+$ central memory T cells (C) in the spleen. (D, E) Quantification of the $CD8^+$ effector memory T cells (D) and $CD8^+$ central memory T cells (E) in the spleen. (F) Photographs of the lungs upon a variety of treatment. The error bars (n = 5) represent means ± SD. (*$p < 0.05$, **$p < 0.01$, ***$p < 0.001$.)

program of PDT scheme to conclude compelling anti-tumor outcomes.

Notes

The authors declare no competing financial interest.

Ethical statement

All the animal experiments involved in this study were conducted in accordance with the Guide for the Care and Use of Laboratory Animals published by the US National Institutes of Health (8th edition, 2011) and approved by the local research ethics review board of the Animal Ethics Committee of Dalian University of Technology (certificate number/ethics approval no. 2020–034).

CRediT authorship contribution statement

Shuang Zeng: Conceptualization, Methodology, Investigation, Visualization, Writing – original draft. **Chen Chen:** Methodology, Visualization, Writing – review & editing. **Liuwei Zhang:** Methodology. **Xiaosheng Liu:** Investigation. **Ming Qian:** Methodology. **Hongyan Cui:** Investigation. **Jingyun Wang:** Conceptualization, Writing – review & editing, Funding acquisition. **Qixian Chen:** Conceptualization, Writing – review & editing, Funding acquisition. **Xiaojun Peng:** Conceptualization, Writing – review & editing.

Declaration of competing interest

The authors declare that they have no known competing financial interests or personal relationships that could have appeared to influence the work reported in this paper.

Acknowledgements

This research was partially funded by National Natural Science Foundation of China (No. 22078050), Fundamental Research Funds for the Central Universities [No. DUT17RC(3)059, DUT20YG126], Dalian Science&Technology Innovation Fund (2020JJ26SN050, 2020JJ26GX025) and Talent Project of Revitalizing Liaoning (XLYC1807184).

Appendix A. Supplementary data

Supplementary data to this article can be found online at https://doi.org/10.1016/j.bioactmat.2022.07.016.

References

[1] R. Siegel, K. Miller, H. Fuchs, A. Jemal, Cancer statistics, 2021, CA A Cancer J. Clin. 71 (2021) 7–33.
[2] N.K. Speicher, N. Pfeifer, Integrating different data types by regularized unsupervised multiple kernel learning with application to cancer subtype discovery, Bioinformatics 31 (2015) i268–i275.
[3] M.C. Luna, C.J. Gomer, Isolation and initial characterization of mouse tumor cells resistant to porphyrin-mediated photodynamic therapy, Cancer Res. 51 (1991) 4243–4249.
[4] J. Kralova, M. Kolar, M. Kahle, J. Truksa, S. Lettlova, K. Balusikova, P. Bartunek, Glycol porphyrin derivatives and temoporfin elicit resistance to photodynamic therapy by different mechanisms, Sci. Rep. 7 (2017), 44497.
[5] Z. Li, J. Jiang, Z. Wang, J. Zhang, M. Xiao, C. Wang, Y. Lu, Z. Qin, Endogenous interleukin-4 promotes tumor development by increasing tumor cell resistance to apoptosis, Cancer Res. 68 (2008) 8687–8694.
[6] Y.Y. Wang, X.L. Liu, R. Zhao, Induction of pyroptosis and its implications in cancer management, Front. Oncol. 9 (2019) 971.
[7] X. Chen, W.T. He, L. Hu, J. Li, Y. Fang, X. Wang, X. Xu, Z. Wang, K. Huang, J. Han, Pyroptosis is driven by non-selective gasdermin-D pore and its morphology is different from MLKL channel-mediated necroptosis, Cell Res. 26 (2016) 1007–1020.
[8] P. Broz, P. Pelegrin, F. Shao, The gasdermins, a protein family executing cell death and inflammation, Nat. Rev. Immunol. 20 (2020) 143–157.
[9] Q. Wang, Y. Wang, J. Ding, C. Wang, X. Zhou, W. Gao, H. Huang, F. Shao, Z. Liu, A bioorthogonal system reveals antitumour immune function of pyroptosis, Nature 579 (2020) 421–426.
[10] Y. Liu, W. Zhen, Y. Wang, S. Song, H. Zhang, Na2S2O8 nanoparticles trigger antitumor immunotherapy through reactive Oxygen species storm and surge of tumor osmolarity, J. Am. Chem. Soc. 142 (2020) 21751–21757.
[11] H. Xiong, X. Ma, X. Wang, W. Su, L. Wu, T. Zhang, Z. Xu, Z.J. Sun, Inspired epigenetic modulation synergy with adenosine inhibition elicits pyroptosis and potentiates cancer immunotherapy, Adv. Funct. Mater. 31 (2021), 2100007.
[12] N. Pizato, B.C. Luzete, L.F.M.V. Kiffer, L.H. Corrêa, I. de Oliveira Santos, J.A. F. Assumpção, M.K. Ito, K.G. Magalhães, Omega-3 docosahexaenoic acid induces pyroptosis cell death in triple-negative breast cancer cells, Sci. Rep. 8 (2018) 1952.
[13] Z. Zhou, H. He, K. Wang, X. Shi, Y. Wang, Y. Su, Y. Wang, D. Li, W. Liu, Y. Zhang, L. Shen, W. Han, L. Shen, J. Ding, F. Shao, Granzyme A from cytotoxic lymphocytes cleaves GSDMB to trigger pyroptosis in target cells, Science 368 (2020) 965.
[14] X. Su, W.J. Wang, Q. Cao, H. Zhang, B. Liu, Y. Ling, X. Zhou, Z.W. Mao, A carbonic anhydrase IX (CAIX)-Anchored rhenium(I) photosensitizer evokes pyroptosis for enhanced anti-tumor immunity, Angew. Chem. Int. Ed. 61 (2022), e202115800.
[15] N. Vasan, J. Baselga, D.M. Hyman, A view on drug resistance in cancer, Nature 575 (2019) 299–309.
[16] L. Jiang, L. Li, X. He, Q. Yi, B. He, J. Cao, W. Pan, Z. Gu, Overcoming drug-resistant lung cancer by paclitaxel loaded dual-functional liposomes with mitochondria targeting and pH-response, Biomaterials 52 (2015) 126–139.
[17] C. He, C. Poon, C. Chan, S.D. Yamada, W. Lin, Nanoscale coordination polymers codeliver chemotherapeutics and siRNAs to eradicate tumors of cisplatin-resistant ovarian Cancer, J. Am. Chem. Soc. 138 (2016) 6010–6019.
[18] S.B. Brown, E.A. Brown, I. Walker, The present and future role of photodynamic therapy in cancer treatment, Lancet Oncol. 5 (2004) 497–508.
[19] M. Li, Y. Shao, J.H. Kim, Z. Pu, X. Zhao, H. Huang, T. Xiong, Y. Kang, G. Li, K. Shao, J. Fan, J.W. Foley, J.S. Kim, X. Peng, Unimolecular photodynamic O_2-economizer to overcome hypoxia resistance in phototherapeutics, J. Am. Chem. Soc. 142 (2020) 5380–5388, 2020.
[20] M. Li, T. Xiong, J. Du, R. Tian, M. Xiao, L. Guo, S. Long, J. Fan, W. Sun, K. Shao, X. Song, J.W. Foley, X. Peng, Superoxide radical photogenerator with amplification effect: surmounting the achilles' heels of photodynamic oncotherapy, J. Am. Chem. Soc. 141 (2019) 2695–2702.
[21] V.N. Nguyen, S. Qi, S. Kim, N. Kwon, G. Kim, Y. Yim, S. Park, J. Yoon, An emerging molecular design approach to heavy-atom-free photosensitizers for enhanced photodynamic therapy under hypoxia, J. Am. Chem. Soc. 141 (2019) 16243–16248.
[22] A.P. Castano, P. Mroz, M.R. Hamblin, Photodynamic therapy and anti-tumour immunity, Nat. Rev. Cancer 6 (2006) 535–545.
[23] J. Jiang, Y. Qian, Z. Xu, Z. Lv, P. Tao, M. Xie, S. Liu, W. Huang, Q. Zhao, Enhancing singlet oxygen generation in semiconducting polymer nanoparticles through fluorescence resonance energy transfer for tumor treatment, Chem. Sci. 10 (2019) 5085–5094.
[24] X. Zhao, S. Long, M. Li, J. Cao, Y. Li, L. Guo, W. Sun, J. Du, J. Fan, X. Peng, Oxygen-dependent regulation of excited-state deactivation process of rational photosensitizer for smart phototherapy, J. Am. Chem. Soc. 142 (2020) 1510–1517.
[25] J. Xia, M. Qian, Q. Yao, Z. Meng, H. Cui, L. Zhang, Y. Li, S. Wu, J. Wang, Q. Chen, X. Peng, Synthetic infrared nano-photosensitizers with hierarchical zoom-in target-delivery functionalities for precision photodynamic therapy, J. Contr. Release 334 (2021) 263–274.
[26] R. Wang, K.H. Kim, J. Yoo, X. Li, N. Kwon, Y.H. Jeon, S.K. Shin, S.S. Han, D.S. Lee, J. Yoon, A nanostructured phthalocyanine/albumin supramolecular assembly for fluorescence turn-on imaging and photodynamic immunotherapy, ACS Nano 16 (2022) 3045–3058.
[27] B. Zhou, J.Y. Zhang, X.S. Liu, H.Z. Chen, Y.L. Ai, K. Cheng, R.Y. Sun, D. Zhou, J. Han, Q. Wu, Tom20 senses iron-activated ROS signaling to promote melanoma cell pyroptosis, Cell Res. 28 (2018) 1171–1185.
[28] K. Nakahira, J.A. Haspel, V.A. Rathinam, S.J. Lee, T. Dolinay, H.C. Lam, J. A. Englert, M. Rabinovitch, M. Cernadas, H.P. Kim, K.A. Fitzgerald, S.W. Ryter, A. M. Choi, Autophagy proteins regulate innate immune responses by inhibiting the release of mitochondrial DNA mediated by the NALP3 inflammasome, Nat. Immunol. 12 (2011) 222–230.
[29] K. Shimada, T.R. Crother, J. Karlin, J. Dagvadorj, N. Chiba, S. Chen, V. K. Ramanujan, A.J. Wolf, L. Vergnes, D.M. Ojcius, A. Rentsendorj, M. Vargas, C. Guerrero, Y. Wang, K.A. Fitzgerald, D.M. Underhill, T. Town, M. Arditi, Oxidized mitochondrial DNA activates the NLRP3 inflammasome during apoptosis, Immunity 36 (2012) 401–414.
[30] R. Zhou, A. Tardivel, B. Thorens, I. Choi, J. Tschopp, Thioredoxin-interacting protein links oxidative stress to inflammasome activation, Nat. Immunol. 11 (2010) 136–140.
[31] X. Zhao, Y. Huang, G. Yuan, K. Zuo, Y. Huang, J. Chen, J. Li, J. Xue, A novel tumor and mitochondria dual-targeted photosensitizer showing ultra-efficient photodynamic anticancer activities, Chem. Commun. 55 (2019) 866–869.
[32] K. Han, Q. Lei, S.B. Wang, J.-J. Hu, W.X. Qiu, J.Y. Zhu, W.N. Yin, X. Luo, X. Z. Zhang, Dual-Stage-Light-Guided tumor inhibition by mitochondria-targeted photodynamic therapy, Adv. Funct. Mater. 25 (2015) 2961–2971.
[33] R. Wang, X.S. Li, J. Yoon, Organelle-targeted photosensitizers for precision photodynamic therapy, ACS Appl. Mater. Interfaces 13 (2021) 19543–19571.
[34] W. Zhai, Y. Zhang, M. Liu, H. Zhang, J. Zhang, C. Li, Universal scaffold for an activatable photosensitizer with completely inhibited photosensitivity, Angew. Chem., Int. Ed. Engl. 58 (2019) 16601–16609.

[35] H. Chen, J. Wang, X. Feng, M. Zhu, S. Hoffmann, A. Hsu, K. Qin, D. Huang, F. Zhao, W. Liu, H. Zhang, Z. Cheng, Mitochondria-targeting fluorescent molecules for high efficiency cancer growth inhibition and imaging, Chem. Sci. 10 (2019) 7946–7951.
[36] C. Zhou, C. Peng, C. Shi, M. Jiang, J.H.C. Chau, Z. Liu, H. Bai, R.T.K. Kwok, J.W. Y. Lam, Y. Shi, B.Z. Tang, Mitochondria-specific aggregation-induced emission luminogens for selective photodynamic killing of fungi and efficacious treatment of keratitis, ACS Nano 15 (2021) 12129–12139.
[37] C.R. Lammert, E.L. Frost, C.E. Bellinger, A.C. Bolte, C.A. McKee, M.E. Hurt, M. J. Paysour, H.E. Ennerfelt, J.R. Lukens, AIM2 inflammasome surveillance of DNA damage shapes neurodevelopment, Nature 580 (2020) 647–652.
[38] V.I. Maltez, A.L. Tubbs, K.D. Cook, Y. Aachoui, E.L. Falcone, S.M. Holland, J. K. Whitmire, E.A. Miao, Inflammasomes coordinate pyroptosis and natural killer cell cytotoxicity to clear infection by a ubiquitous environmental bacterium, Immunity 43 (2015) 987–997.
[39] S.M. Man, R. Karki, T.D. Kanneganti, Molecular mechanisms and functions of pyroptosis, inflammatory caspases and inflammasomes in infectious diseases, Immunol. Rev. 277 (2017) 61–75.
[40] V.M. Ringel-Scaia, N. Beitel-White, M.F. Lorenzo, R.M. Brock, K.E. Huie, S. Coutermarsh-Ott, K. Eden, D.K. McDaniel, S.S. Verbridge, J.H. Rossmeisl Jr., K. J. Oestreich, R.V. Davalos, I.C. Allen, High-frequency irreversible electroporation is an effective tumor ablation strategy that induces immunologic cell death and promotes systemic anti-tumor immunity, EBioMedicine 44 (2019) 112–125.
[41] Z. Zhang, Y. Zhang, S. Xia, Q. Kong, S. Li, X. Liu, C. Junqueira, K.F. Meza-Sosa, T.M. Y. Mok, J. Ansara, S. Sengupta, Y. Yao, H. Wu, J. Lieberman, Gasdermin E suppresses tumour growth by activating anti-tumour immunity, Nature 579 (2020) 415–420.
[42] H. Deng, Z. Zhou, W. Yang, L.S. Lin, S. Wang, G. Niu, J. Song, X. Chen, Endoplasmic reticulum targeting to amplify immunogenic cell death for cancer immunotherapy, Nano Lett. 20 (2020) 1928–1933.
[43] J. Li, H. Gao, R. Liu, C. Chen, S. Zeng, Q. Liu, D. Ding, Endoplasmic reticulum targeted AIE bioprobe as a highly efficient inducer of immunogenic cell death, Sci. China Chem. 63 (2020) 1428–1434.
[44] C. Chen, X. Ni, S. Jia, Y. Liang, X. Wu, D. Kong, D. Ding, Massively evoking immunogenic cell death by focused mitochondrial oxidative stress using an AIE luminogen with a twisted molecular structure, Adv. Mater. 31 (2019), 1904914.
[45] B. Feng, Z. Niu, B. Hou, L. Zhou, Y. Li, H. Yu, Enhancing T riple negative breast cancer immunotherapy by ICG-T emplated self-assembly of paclitaxel nanoparticles, Adv. Funct. Mater. 30 (2020), 1906605.
[46] S. Ma, W. Song, Yudi Xu, X. Si, S. Lv, Y. Zhang, Z. Tang, X. Chen, Rationally designed polymer conjugate for tumor-specific amplification of oxidative stress and boosting antitumor immunity, Nano Lett. 20 (2020) 2514–2521.
[47] S. Spranger, R.M. Spaapen, Y. Zha, J. Williams, Y. Meng, T.T. Ha, T.F. Gajewski, Up-regulation of PD-L1, ido, and Tregs in the melanoma tumor microenvironment is driven by CD8+ T cells, Sci. Transl. Med. 5 (2013), 200ra116.